Superiorized method for metal artifact reduction

Thomas Humphries* and Boyang (Jessie) Wang
School of STEM, University of Washington Bothell,
Box 358538, 18115 Campus Way NE, Bothell, WA, 98011
(Dated: June 9, 2020)

Purpose: Metal artifact reduction (MAR) is a challenging problem in computed tomography (CT) imaging. A popular class of MAR methods replace sinogram measurements that are corrupted by metal with artificial data, typically generated from some combination of interpolation along with other heuristics. While these "projection completion" approaches are successful in eliminating severe artifacts, secondary artifacts may be introduced by the artificial data. In this paper, we propose an approach which uses projection completion to generate a prior image, which is then incorporated into an iterative reconstruction algorithm based on the superiorization framework. The rationale is that the image produced by the iterative algorithm can inherit the desirable properties of the prior image, while also reducing secondary artifacts.

Methods: The prior image is reconstructed using normalized metal artifact reduction (NMAR), a popular projection completion approach. The iterative algorithm is a modified version of the simultaneous algebraic reconstruction technique (SART), which reduces artifacts by incorporating a polyenergetic forward model, least-squares weighting, and superiorization. The penalty function used for superiorization is a weighted average between a total variation (TV) term and a term promoting similarity with the prior image, similar to penalty functions used in prior image constrained compressive sensing (PICCS). Because the prior is largely free of severe metal artifacts, these artifacts are discouraged from arising during iterative reconstruction; additionally, because the iterative approach uses the original projection data, it is able to recover information that is lost during the NMAR process.

Results: We perform numerical experiments modeling a simple geometric object, as well as several more realistic scenarios such as metal pins, bilateral hip implants, and dental fillings placed within an anatomical phantom. The proposed iterative algorithm is largely successful at eliminating severe metal artifacts as well as secondary artifacts introduced by the NMAR process, especially lost edges of bone structures in the neighborhood of the metal regions. In one case modeling severe photon starvation, the NMAR algorithm is found to provide better results.

Conclusion: The proposed algorithm is effective in applying the superiorization methodology to the problem of MAR, providing better results than both NMAR and a purely total variation-based superiorization approach in nearly all cases.

I. INTRODUCTION

Artifacts caused by metal objects, such as prostheses, rods, screws, and fillings, are a well-known source of image artifacts in computed tomography (CT). These artifacts are caused by numerous physical factors, including beam hardening, increased measurement noise, photon starvation, partial volume and exponential edge gradient effects, and scatter [1]. They typically appear as dark streaks or bands between metal objects, as well as thin, alternating dark and light streaks emanating from these objects. These artifacts tend to be dramatic and may obscure important features of the image.

Despite the long history of proposed metal artifact reduction (MAR) techniques (see Ref. [2] for a recent review), it remains a challenging problem. Dual-energy systems are able to significantly reduce metal artifacts [3], but require special equipment. On conventional systems, a common approach, often referred to as projection completion, regards measurements that have passed through a metal object as unreliable, and replaces them with arti-

ficially generated data. Typically, a preliminary, artifact corrupted image is first reconstructed from the raw sinogram to identify metal regions in the image space, followed by a simulated forward projection to identify the so-called metal trace in the sinogram domain. Once data inside the metal trace have been replaced, an image is reconstructed from the modified data using a standard technique such as filtered backprojection (FBP).

Early projection completion methods [4,5] used linear interpolation (LI) to replace the metal trace within each column of the sinogram. While the LI approach is effective in removing the most severe metal artifacts, it also produces secondary artifacts, due mainly to the loss of edge information about other structures (e.g. bone or air pockets) where their traces intersect with the metal trace [6]. A popular way to address this issue is to use the preliminary image to not only identify the metal trace, but also generate a prior image, which omits metal but retains information about the other structures such as bone. A number of authors [7–14] propose replacing the metal trace with the corresponding measurements obtained from simulated forward projection of the prior, rather than LI data. Alternatively, in normalized metal artifact reduction (NMAR) methods, the prior is used to normalize the projections [6,15,16] before a sinogram

* Email: thumphri@uw.edu

correction using LI; the sinogram is subsequently "de-normalized" to reintroduce lost edge information. The prior image is typically generated using tissue classification of an image reconstructed using FBP [7–9,15] or by iterative reconstruction with regularization to suppress artifacts [10–13,17]; one recent work [14] has also proposed generating the prior using a convolutional neural network.

Some approaches based on projection completion employ additional heuristics to reduce secondary artifacts. Ref. [18] proposes segmenting bone from the preliminary reconstruction (replacing bone pixels with smoothed soft tissue values) and then reintroducing bone to the image after an interpolation-based projection completion is performed. Ref. [19] uses a distance-dependent spatial weighting to combine the LI image with one processed using multi-dimensional adaptive filtering to reduce noise. Ref. [20] begins with an LI reconstruction and then performs several iterations in which the reconstruction is forward projected, averaged with experimental data using spatial weighting, then reconstructed again. Other methods retain edge information by performing projection completion in the Fourier [21] or wavelet [22–24] domains, rather than on the original sinogram. Another recent approach [25] uses a convolutional neural network to combine information from an NMAR image and the uncorrected image. Finally, projection completion can also be performed directly in the sinogram domain without reconstruction of a preliminary image [26], avoiding issues of mismatch between the simulated forward projection and true system geometry.

An alternative to projection completion is to use the original data and reconstruct the image using an iterative algorithm. Iterative algorithms, while more computationally expensive than FBP, have the advantage of being able to accurately model physical effects contributing to metal artifacts, such as beam hardening and noise. They also may be able to solve the exterior problem (where the metal-corrupted data are ignored rather than replaced) with the inclusion of regularization terms to mitigate the ill-posedness of the problem. Ref. [27] applied both the algebraic reconstruction technique (ART) and expectation maximization (EM), finding that both outperformed FBP reconstruction. Later work has incorporated polyenergetic modeling into the EM framework [28,29], applied EM to projection completed data [30], used ART in conjunction with total variation (TV) penalties [31,32] and used optimization-based reconstruction with machine-learned regularization [24]. In Ref. [33], the authors simultanously estimate the image and the mismatch between polyenergetic and (idealized) monoenergetic data, using a regularized least squares approach incorporating a prior image and several different regularizers.

Projection completion approaches and iterative methods each have advantages and disadvantages. Projection completion is especially effective in removing severe streaking artifacts from images, but the use of artificially generated data carries an inherent risk of creating new artifacts. Iterative methods can make use of the original projection data, but the poor quality of the metal contaminated measurements make obtaining a high quality image difficult. In this paper we combine projection completion with an iterative method to attempt to mitigate these issues. We use the NMAR method to construct a prior image which is free of severe artifacts, but may contain some secondary artifacts. This image is then used both as the initial estimate and as a prior in an iterative method which reconstructs an image from the original projection data. The iterative method incorporates the superiorization methodology [34] with a secondary objective guided by the prior image as well as a total variation (TV) minimization term. Numerical experiments indicate that the proposed algorithm is successful in eliminating both severe artifacts due to streaking, as well as secondary artifacts introduced during the NMAR process.

II. MATERIALS AND METHODS

A. Mathematical model

We consider a two-dimensional attenuation distribution, $\mu(y, E) : \mathbb{R}^2 \times \mathbb{R} \to \mathbb{R}$, which depends on position, y, and the energy of the incident X-ray beam, E. If the X-ray beam is monoenergetic with energy E_0, the idealized measurement along a line j is modeled as

$$\widehat{I}_j = I_0 \exp\left(-\int_j \mu(y, E_0)\, dy\right), \qquad (1)$$

where I_0 is the initial intensity of the beam and $\widehat{I}_j$ is the (idealized) intensity measured by the detector, in counts per second. The line integral, $\int_j \mu(y, E_0)\, dy$, which is a sample from the Radon transform of $\mu(y, E_0)$, can be obtained by log-transforming the data,

$$\ln\left(I_0/\widehat{I}_j\right) = \int_j \mu(y, E_0)\, dy. \qquad (2)$$

Discretizing μ as an image with K pixels, and taking measurements along J lines, then yields a system of linear equations

$$Ax = b, \qquad (3)$$

where $x \in \mathbb{R}^K$ is the discretized image of μ, $b \in \mathbb{R}^J$ is the line integral data, and $A \in \mathbb{R}^{J \times K}$ is the system matrix whose (j, k)th element is the length of intersection of the jth line with the kth pixel of x.

Clinical CT systems, however, generate polyenergetic X-ray beams, with a spectrum of energies typically ranging from zero up to roughly 150 keV (see, e.g., Fig. 1). In this instance, the measurement model is expressed as

$$\widehat{I}_j = \int S(E) \exp\left(-\int_j \mu(y, E)\, dy\right) dE, \qquad (4)$$

where $S(E)$ is the beam spectrum. Log-transforming the data and applying the mean value theorem for integrals then gives

$$\ln\left(I_0/\widehat{I}_j\right) = \int_j \mu(y, E_j)\, dy, \qquad (5)$$

where $I_0 = \int S(E)\, dE$, and E_j is an unknown energy in the range of the spectrum, depending on the path j. The inconsistency with the monoenergetic model (2) leads to so-called beam hardening artifacts [35], including cupping and streaking. From the physical perspective, as the polyenergetic beam passes through the object, photons with lower energy are attenuated at a higher rate than photons with greater energy, causing the spectrum of the beam to "harden" as it becomes skewed towards higher energies. Metal objects induce particularly severe beam hardening artifacts due to their high attenuation coefficients, particularly at the low end of the energy spectrum.

Another contributing factor to metal artifacts is increased image noise. Due to the stochastic nature of X-ray interactions with matter, the measurement along line j is typically modeled as a Poisson random variable I_j, with mean equal to $\widehat{I}_j$. The measurement therefore has a signal-to-noise ratio (SNR) of $\sqrt{\widehat{I}_j}$; i.e., the SNR deteriorates as $\widehat{I}_j$ becomes small. This situation occurs if the initial beam intensity $\int S(E)\, dE$ is small, or if the line integral through $\mu(y, E)$ is large. Measurements passing through metal objects thus tend to be very noisy, degrading image quality. In the extreme case $\widehat{I}_j$ may be so small that $I_j = 0$ (no counts are detected along the line), resulting in an effective attenuation measurement of infinity.

B. Beam hardening and metal artifact reduction

A standard approach to reduce beam hardening artifacts is to perform water correction (sometimes known as soft tissue correction) on the measured data [36]. Water correction (Algorithm 1) simulates a monoenergetic measurement m_j from the corresponding polyenergetic measurement I_j via a two step process. First, the effective length, T_j, of water through which the polyenergetic beam would have to pass to generate I_j is estimated. This can be accomplished by solving a nonlinear equation (Line 3 of Algorithm 1, with $\mu_w(E)$ denoting the attenuation coefficient of water) or, more commonly, by interpolating from a table of measured values based on known thicknesses of water. Once T_j is known, the corresponding measurement m_j at some reference energy E_0 can be obtained straightforwardly.

Water correction essentially assumes that the object consists only of water or water-like materials. This assumption breaks down if the object contains dense material like bone, contrast agents, or metal, whose attenuation curves do not behave like scaled versions of the

---

Algorithm 1: Water correction.

1   *Given:* Polyenergetic measurements I_j, $j \in [1, J]$.

2   **for** $j = 1$ *to* J **do**
3   Solve $I_j = \int S(E) \exp(-\mu_w(E) T_j)\, dE$ for T_j;
4   Set $m_j = I_0 \exp(-\mu_w(E_0) T_j)$;
5   **end**
6   **return** $m_j, j \in [1, J]$.

---

attenuation curve of water. Water correction is therefore effective in reducing cupping artifacts, but not the so-called second-order artifacts caused by those materials. Correcting for these artifacts typically requires more advanced data corrections [36–38] or iterative methods which directly model polyenergetic X-rays [28,39–41].

As discussed in the Introduction, a standard method of metal artifact reduction (MAR) is to replace metal-contaminated measurements with linearly interpolated data [4,5]. Pseudocode for this method, which we denote as MAR, is provided in Algorithm 2. A preliminary image x_{uncorr} is reconstructed from the water corrected sinogram, and the image is segmented into nonmetal and metal parts using thresholding. The metal index $\mathbf{1_m}$ is forward projected to obtain the metal trace in the sinogram domain. The sinogram is then processed columnwise (i.e. with respect to each projection angle) to replace measurements corresponding to the metal trace with their interpolated values. An image can then be reconstructed from the corrected sinogram, and the metal objects can be re-inserted if desired.

Algorithm 2: MAR method

1   *Given:* Water-corrected sinogram, b_{mono}, and system matrix, A.

2   Reconstruct image x_{uncorr} from b_{mono};
3   Segment x_{uncorr} to obtain metal index $\mathbf{1_m}$;
4   Set $trace = A\, \mathbf{1_m}$ (forward projection);
5   Set $b_{mono} = 0$ wherever $trace > 0$;
6   **for** *every column of* b_{mono} **do**
7   Fill in zero values by linear interpolation to obtain corresponding column of b_{MAR};
8   **end**
9   **return** b_{MAR}

The MAR method reduces severe artifacts caused by metal, but produces secondary artifacts, as the interpolation results in the loss of edge information about other structures. The normalized metal artifact reduction (NMAR) method [15] (Algorithm 3) addresses this issue through the use of a prior image. Following the preliminary reconstruction, x_{uncorr} is segmented into air, soft tissue, bone, and metal. The prior image is created by setting regions containing air and soft tissue to their respective attenuation values at the reference energy. Regions containing bone are assigned the corresponding attenuation coefficients from x_{uncorr}, to accurately capture

the varying attenuation of bone. The values assigned to the metal regions are unimportant [15]; we use soft tissue for simplicity. The prior image is then forward projected, and the resulting sinogram b_{prior} is divided elementwise ($\oslash$) into the original sinogram to normalize it. The MAR algorithm is then applied to the normalized sinogram, followed by an elementwise multiplication ($\otimes$) with b_{prior} to "de-normalize" the sinogram. The de-normalization step effectively recovers edge information about bone and other structures that may be lost during the MAR step [6,15].

Fig. 1 highlights the differences between MAR and NMAR. In the sinogram profiles (top right) we can observe that the interpolated profile used by MAR (red line) does not accurately capture the traces of the bone and air pocket, while the NMAR method does. While the MAR correction (bottom center) removes the large streak between the two metal objects that appears in the water corrected (bottom left) image, secondary streaking artifacts are created between the metal objects and the bone and air pockets. NMAR is able to remove virtually all artifacts in this simple experiment, though a mild artifact persists surrounding the bone region.

Algorithm 3: NMAR method

---

1 *Given:* Water-corrected sinogram, b_{mono}, system matrix, A, reference energy E_0.

2 Reconstruct image x_{uncorr} from b_{mono};

3 Segment x_{uncorr} to obtain indices $\mathbf{1_a}, \mathbf{1_s}, \mathbf{1_b}$ and $\mathbf{1_m}$ (air, soft tissue, bone, metal);

4 Set $x_{prior} = \mu_a(E_0)$ wherever $\mathbf{1_a} = 1$;

5 Set $x_{prior} = \mu_s(E_0)$ wherever $\mathbf{1_s} \cup \mathbf{1_m} = 1$;

6 Set $x_{prior} = x_{uncorr}$ wherever $\mathbf{1_b} = 1$;

7 $b_{prior} = Ax_{prior}$;

8 $b_{norm} = b_{mono} \oslash b_{prior}$;

9 $b_{MAR} = MAR(b_{norm}, A)$;

10 $b_{NMAR} = b_{MAR} \otimes b_{prior}$;

11 return b_{NMAR}

C. Iterative reconstruction

Standard iterative reconstruction methods are based on solving the linear system $Ax = b$ as described in (3). Our approach is based on a block-iterative variant of the simultaneous algebraic reconstruction technique (SART) [42], as described in Ref. [43]. We first define diagonal matrices D and M as:

$$D \in \mathbb{R}^{K \times K}, \ D_{kk} = 1 \Big/ \sum_{i=1}^{J} |a_{ik}|$$

$$M \in \mathbb{R}^{J \times J}, \ M_{jj} = 1 \Big/ \sum_{i=1}^{K} |a_{ji}|$$

To implement block iteration, the columns of the sinogram are evenly partitioned into N_w subsets, indexed by

w; for example, if $N_w = 5$, then $w = 1$ would correspond to the first, sixth, eleventh, etc. columns, $w = 2$ to the second, seventh, twelfth, and so on.This accelerates the convergence of the algorithm. One iteration of the block iterative SART (BI-SART) algorithm is then given by

$$x^{(i+1)} = \mathbf{Q}\mathbf{B}_{N_w} \dots \mathbf{B}_2 \mathbf{B}_1(x^{(i)}), \text{where} \quad (6)$$

$$\mathbf{B}_w(x) = x - D_w(A_w)^T M_w [A_w x - b_w], \quad (7)$$

$$(\mathbf{Q}x)_k = \max\{0, x_k\}, \quad k \in [1, K].$$

The subscript w indicates that only rows of A and b corresponding to the measurements in w are used, including when forming the matrices D_w and M_w. The operator $\mathbf{Q}$ ensures non-negativity of the solution after every iteration.

The BI-SART algorithm accounts for neither the statistical uncertainty in the measured data, nor the polyenergetic nature of the X-ray measurements. Additionally, images reconstructed by BI-SART may be of poor quality when the data are noisy. In Ref. [44], we introduced three enhancements to the BI-SART algorithm to address these issues, which are especially important in the context of metal artifact reduction. We summarize these enhancements below:

1. Polyenergetic forward model

To account for the polyenergetic measurements, we adopt the polyenergetic SART (pSART) method [45]. pSART defines a polyenergetic forward projection operation $\mathcal{P}$ using linear interpolation between tabulated attenuation curves for known basis materials such as soft tissue, bone, and metal. Specifically, letting x denote the attenuation image at the reference energy E_0, we define

$$\mu(x_k, E) = \frac{[\mu_{m+1}(E_0) - x_k]\mu_m(E) + [x_k - \mu_m(E_0)]\mu_{m+1}(E)}{\mu_{m+1}(E_0) - \mu_m(E_0)}, \quad (8)$$

where $\mu_m(E)$ and $\mu_{m+1}(E)$ are the linear attenuation coefficient (LAC) curves of the two basis materials whose LACs at E_0 bracket the pixel value x_k. For example, if x_k has an LAC halfway between that of soft tissue and bone at E_0, its LAC is assumed to be halfway between that of soft tissue and bone at all other energies as well. The polyenergetic forward projection operation is then defined as

$$[\mathcal{P}(x)]_j = \ln \left[\sum_{h=1}^{N_h} S_h \Big/ \sum_{h=1}^{N_h} S_h \exp\left(-a_j \mu(x, E_h)\right) \right], \quad (9)$$

where S_h is a discretization of the continuous beam spectrum $S(E)$ into N_h energy levels, and a_j is the jth row of A (cf. (4) and (5)). The pSART iteration is achieved by simply replacing the monoenergetic forward projection Ax in SART with $\mathcal{P}(x)$ in (7).:

$$\mathbf{B}_w(x) = x - D_w(A_w)^T M_w [\mathcal{P}_w(x) - b_w]. \quad (10)$$

While pSART has not been proven to converge in general, it has been shown to be effective in reducing beam hardening artifacts in numerical experiments [45–47].

2. Weighted least squares

To model measurement uncertainty, a weighted least squares approach (WLS) [48] can be employed. We define the diagonal weighting matrix as

$$W \in \mathbb{R}^{J \times J}, \ W_{jj} = I_j, \quad (11)$$

We can then apply BI-SART to the system $W^{\frac{1}{2}} A x = W^{\frac{1}{2}} b$, which assigns proportionally higher weight to the less noisy measurements. Incorporating the polyenergetic forward projection as well, the modified iteration is given by

$$\mathbf{B}_w(x) = x - D'_w(A_w)^T M_w \left[W_w^{\frac{1}{2}} \left(\mathcal{P}_w(x) - b_w \right) \right], \quad (12)$$

where $D'_{kk} = 1 \Big/ \sum_{i=1}^{J} \left| (W^{\frac{1}{2}} A)_{ik} \right|$. Matrix M does not need to be modified, as the factor of $W^{\frac{1}{2}}$ is cancelled during multiplication with $(W^{\frac{1}{2}} A)^T$.

3. Superiorization

Superiorization [34] is an optimization heuristic in which solutions generated by an iterative algorithm are perturbed in every iteration, to improve the quality of the solution in some respect. For example, if (6) is taken to be the basic iterative algorithm with $\mathbf{B}_w$ defined in (12), then the superiorized version is of the form

$$x^{(i+1)} = \mathbf{Q} \mathbf{B}_{N_w} \ldots \mathbf{B}_2 \mathbf{B}_1(x^{(i)}, + \beta^{(i)} v^{(i)}), \quad (13)$$

where $\beta^{(i)} > 0$, $\sum_i \beta^{(i)} < \infty$, and the $v^{(i)}$ are a sequence of bounded perturbation vectors. The key result underlying superiorization is that if the basic algorithm is *perturbation resilient*, the superiorized version is able to find a solution that is equally satisfactory with respect to satisfying the constraints of the problem ($\mathcal{P}(x) = b$ in our case), though typically this requires more iterations. The perturbation vectors are usually chosen to be nonascending directions of some penalty function $\phi(x)$ at the current iterate, for example, $v^{(i)} = -\nabla \phi(x^{(i)}) / \|\nabla \phi(x^{(i)})\|$. Thus, the solution found by the superiorized algorithm can be expected to be superior with respect to ϕ, while equally compatible with the constraints. The methodology has been featured in a special edition of *Inverse Problems* [49], and a continuously updated online bibliography is maintained at http://math.haifa.ac.il/YAIR/bib-superiorization-censor.html.

All three of the proposed enhancements (polyenergetic forward projection, weighted least squares, and superiorization) can be implemented independently of one another. In [47] we found that polyenergetic forward projection and TV superiorization could be used to eliminate beam hardening artifacts as well as artifacts due to sparse-view and limited-angle data. In [44], we found that including all three enhancements in the reconstruction algorithm provided the best results when metal artifacts were present. Pseudocode for this algorithm is presented in Algorithm 4. In the implementation of the algorithm, we allow for a total of N perturbations to be applied in every iteration, to further improve the solution with respect to the penalty function. (This is of course equivalent to a single perturbation, albeit one that cannot be determined *a priori*). The step sizes decrease geometrically with rate $0 < \gamma < 1$ to ensure that the perturbations are summable.

In [44], total variation (TV) was used as the penalty function employed by superiorization:

$$\phi_{TV}(x) = \sum_{m,n} \sqrt{(x_{m+1,n} - x_{m,n})^2 + (x_{m,n+1} - x_{m,n})^2 + \epsilon^2}, \quad (14)$$

where $x_{m,n}$ denotes the pixel in the mth row and nth column of the image x. The small parameter ϵ is introduced to avoid singularity of $\nabla \phi_{TV}$ at points where the image is piecewise constant. While the algorithm, which we denoted as wPSART-TV (weighted polyenergetic SART with TV superiorization) was effective in reducing metal artifacts, we found that it was difficult to remove strong streaking artifacts between metal objects; for example, in the case of a bilateral hip implant. This was especially true at low count rates, where photon starvation was a significant factor. This motivates the development of the hybrid algorithm, discussed in the next section.

D. Prior image constrained superiorized algorithm

Our prior image constrained superiorized algorithm (Algorithm 5), which we denote as wPSART-PICS, consists of several steps, highlighted in Fig. 2. First, the water corrected sinogram is corrected using NMAR to obtain a metal corrected sinogram. A modified version of Algorithm 4 is then applied to this sinogram to reconstruct a prior image, x_{prior}. In the modified version of the algorithm, monoenergetic forward projection (i.e. multiplication by A) is used instead of $\mathcal{P}$, and the weighting matrix W is omitted, since the data have been water corrected and the noisy metal trace removed by NMAR. Total variation (14) is used as the penalty function for superiorization, in order to generate a smooth prior image.

The prior image is then incorporated into a second penalty function:

$$\phi_{PI}(x) = \alpha \phi_{TV}(x) + (1 - \alpha) \phi_{TV}(x - x_{prior}), \quad (15)$$

Algorithm 4: Block-iterative, weighted, polyenergetic SART with superiorization

---

1 *Given:* Log-transformed polyenergetic sinogram b_{poly}, system matrix A, number of subsets N_w, reference energy E_0, spectrum S, tabulated attenuation curves $\mu_m(E)$, initial image x_0, stopping criteria ε and/or i_{max}, superiorization parameters γ, N.

2 $\ell = -1$;

3 $i = 0$;

4 **while** $\|\mathcal{P}\left(x^{(i)}\right) - b_{poly}\|_2 \geq \varepsilon$ **and** $i < i_{max}$ **do**

5 $\quad n = 0$;

6 $\quad x^{(i,n)} = x_i$;

7 $\quad$ **while** $n < N$ **do**

8 $\quad\quad v^{(i,n)} = -\nabla\phi(x^{(i,n)}) \ / \ \|\nabla\phi(x^{(i,n)})\|_2$;

9 $\quad\quad$ **while true do**

10 $\quad\quad\quad \ell = \ell + 1$;

11 $\quad\quad\quad \beta^{(i,n)} = \gamma^\ell$;

12 $\quad\quad\quad z = x^{(i,n)} + \beta^{(i,n)}v^{(i,n)}$;

13 $\quad\quad\quad$ **if** $z \in \Omega$ *and* $\phi(z) \leq \phi(x^{(i)})$ **then**

14 $\quad\quad\quad\quad x^{(i,n+1)} = z$;

15 $\quad\quad\quad\quad$ **break**;

16 $\quad\quad\quad$ **end**

17 $\quad\quad$ **end**

18 $\quad\quad n = n + 1$;

19 $\quad$ **end**

20 $\quad x^{(i+1)} = \mathbf{Q}\mathbf{B}_{N_w}\ldots\mathbf{B}_2\mathbf{B}_1(x^{(i,N)})$, where $\mathbf{B}_w(x) =$
$\quad\quad x - D'_w(A_w)^T M_w \left[W_w^{\frac{1}{2}}\left(\mathcal{P}_w(x) - b_{poly,w}\right)\right]$;

21 $\quad i = i + 1$;

22 **end**

23 **return** $x^{(i)}$

---

where $\alpha \in [0,1]$ controls the weighting of the two terms. This type of penalty is used in the prior image constrained compressed sensing (PICCS) approach described in [50,51]; we use the term "superiorization" instead of "compressed sensing" as it more accurately describes our method. Algorithm 4 is then applied with the original polyenergetic projection data and $\phi_{PI}(x)$ as the penalty function. The prior image is also used as the initial estimate, as it is expected to be a good approximation to the true image.

Algorithm 5: wPSART-PICS algorithm

---

1 *Given:* Water corrected sinogram b_{mono}, all inputs needed for Algorithm 4.

2 Apply NMAR to b_{mono} to obtain b_{NMAR};

3 Use Algorithm 4 (modified) with b_{NMAR} as sinogram to reconstruct prior image x_{prior};

4 Set $\phi_{PI}(x) = \alpha\phi_{TV}(x) + (1-\alpha)\phi_{TV}(x - x_{prior})$;

5 Use Algorithm 4 with b_{poly} as sinogram, $x_0 = x_{prior}$, and $\phi_{PI(x)}$ as penalty function to reconstruct x_{final};

6 **return** x_{final}

By penalizing the TV of the difference between the re-

constructed image and the prior, $\phi_{PI}(x)$ effectively promotes similar edge structure between the two images. Our motivation for using $\phi_{PI}(x)$ in this application is that if the NMAR-based prior is largely free of severe streaking artifacts, these artifacts will also be penalized in the image being reconstructed. Since the final step of Algorithm 5 uses the original polyenergetic data, however, it should be possible to recover image details that are lost due to the interpolation performed by NMAR.

III. RESULTS

We validated our approach using several numerical experiments. The wPSART-PICS algorithm was implemented in Matlab using the Michigan Image Reconstruction Toolbox (MIRT) [52] to simulate the CT spectrum, material attenuation curves, and generate the system matrix A for iterative reconstruction. We implemented our own version of NMAR in Matlab as well, using the built-in Image Processing Toolbox methods to segment the CT image.

A. Simple phantom experiments

We first generated the simple mathematical phantom shown in Fig. 1 to fine tune the algorithm parameters, before studying more realistic data. The phantom is 400×400 pixels with a pixel size of 0.75 mm. It consists of a background region of soft tissue, two small circular regions containing titanium, and a larger oblong region containing bone. The linear attenuation coefficients of soft tissue, bone and titanium at the reference energy E_0 of 70 keV are 0.203, 0.494, and 2.44 cm^{-1}, respectively. The phantom also consists of an air pocket and several low contrast features (modeled after the Shepp-Logan phantom) in the center of the object. The low-constrast features have attenuation values of $\pm 5\%$ relative to the background, and are heavily obscured by metal streaking artifacts if no metal artifact correction is performed (see Fig. 1).

We analytically computed 720 parallel-beam views over a 180° arc around the phantom. A 130 kVp spectrum was simulated to generate polyenergetic data. Poisson noise was subsequently added to the data, proportionally to initial count rates of $I_0 = 1.0 \times 10^5$, 2.0×10^5, 5.0×10^5, and 1.0×10^6. To reconstruct the data using Algorithm 5, we ran 24 iterations of the modified algorithm (Line 3) to generate x_{prior}. Algorithm 4 was then run for 32 iterations to produce a final image. In both instances, $N_w = 12$ subsets of projection data were used. The parameters controlling the gradient descent steps within the superiorized algorithm were set to $\gamma = 0.9995$, $N = 40$. To test the sensitivity of the resulting image to the choice of α in (15), we performed reconstructions with $\alpha = 1.0, 0.8, 0.5, 0.2$, and 0.0; the first value corresponding to the case of ordinary TV regularization. For

comparison, we also reconstructed an image using the wPSART-TV approach of Ref. [44]; this is equivalent to applying Algorithm 4 with $x_0 = 0$ and $\phi = \phi_{TV}$.

For quantitative comparisons, we defined an $n \times n$ pixel region of interest (ROI) in the center of the object (n=51), surrounding the six small low-contrast features. Pixel values within the ROI were rescaled to the interval $[0, 1]$ using the formula

$$x_{new,k} = \frac{x_{old,k} - x_{min}}{x_{max} - x_{min}}, \tag{16}$$

where x_{min} and x_{max} were set to $\pm 10\%$ of the background soft tissue value. The peak signal-to-noise ratio (PSNR) of the region was then calculated as

$$PSNR = 10 \log_{10}\left(\frac{1}{MSE}\right), \text{where} \tag{17}$$

$$MSE = \frac{1}{n^2} \sum_k \left(x_{true,k} - x_{new,k}\right)^2. \tag{18}$$

The rescaling was performed so that the PSNR values were better able to capture differences between the reconstructed values within the ROI.

Fig. 3 shows the images reconstructed using all approaches at the noise level of $I_0 = 5.0 \times 10^5$. While the prior image reconstructed from the NMAR data (B) is free of metal streaking artifacts, there is a small artifact around the oblong bone region in the bottom right due to inaccuracy in the segmentation applied during NMAR. This artifact is absent from images C–H, which are reconstructed from the original data. Image C, reconstructed using the wPSART-TV algorithm, retains a mild streaking artifact between the two metal objects. This is likely due to the fact that the image is reconstructed without any prior knowledge from the NMAR correction, which removes the streak entirely. Image D begins from $x_0 = x_{prior}$, but uses only TV as the penalty function during superiorized reconstruction (since $\alpha = 1.0$), resulting in blurred edges around the low-contrast features. Images E–H, reconstructed using pSART-PICS with $\alpha < 1$, demonstrate better definition about the features. Images D–H do include a small dark shadow surrounding the two metal objects; this appears to arise as a result of a slight mismatch between metal trace of the forward projection of the prior with the actual sinogram, resulting in large discrepancies in the data domain in a small number of pixels. This results in an overcorrection in the pixels surrounding the metal regions.

The PSNR values given in Table I corroborate these observations. At all four noise levels, the best PSNR values are obtained using wPSART-PICS with an α value of 0.0 (column H). This indicates that (for this experiment, in any event), there is no benefit to including the TV of the image in the penalty function (15). This is perhaps not surprising, since the prior image itself is reconstructed using TV superiorization and is therefore quite smooth itself. That being said, the difference in PSNR values between columns E–H is only on the order of 1–2%,

indicating that the algorithm is not particularly sensitive to the choice of α, as long as $\alpha < 1.0$. Comparatively, the difference in PSNR values between columns D and E ($\alpha = 1.0$ versus $\alpha = 0.8$) ranges from 2 – 10%.

B. Anatomical phantom experiments

To test the performance of the algorithm on more realistic data, slices of clinical CT images were downloaded from the Cancer Imaging Archive (https://www.cancerimagingarchive.net/). Four 512×512 pixel slices were selected from the dataset, representing the abdominal, shoulder, pelvic and head regions. Metal objects representing pins, dental fillings, and a bilateral hip implant were subsequently manually inserted into the image slices; the pins and hip implants were modeled as titanium, while the fillings were modeled as gold. The objects were modeled after those appearing in Ref. [14]. Fan beam data corresponding to 900 views over $360°$ were simulated using the MIRT toolbox, using the same 130 kVp spectrum and reference energy of 70 keV as for the simple phantom experiment. Soft thresholding [14] with base materials of fat, soft tissue, and bone were used to generate attenuation coefficients for nonmetal regions at every energy level when simulating the polyenergetic data. Noise was then added to the data proportional to count rate of $I_0 = 2.0 \times 10^5$. The four true images and their reconstructions using FBP are shown in the first two rows of Fig. 4, illustrating the severity of the metal artifacts when no correction is performed.

Images were reconstructed using the same algorithms as in the previous section. In light of the results from the simple phantom experiment, we only used values of $\alpha = 1.0$, 0.5 and 0.0 for the pSART-PICS algorithm. All superiorized algorithms were run with $\gamma = 0.995$ and $N = 10$; while the choice of $\gamma = 0.9995$, $N = 40$ gave good results for the simple phantom used in the previous section, we found that it tended to oversmooth the images based on real CT data. By reducing both γ and N, we smooth the images less because we perform fewer gradient descent iterations in Algorithm 4, while also reducing the step size more quickly.

For the purposes of comparison, two other reconstruction approches were used. The first is a modified version of Algorithm 5 which uses water corrected data b_{mono} instead of b_{poly} on line 5 of the algorithm, together with the monoenergetic version of Algorithm 4. This approach gives an indication of how the proposed algorithm could be adapted in the case that the beam spectrum is difficult to approximate accurately, as water correction can be performed without knowledge of the spectrum. The second approach is frequency split MAR (FSMAR) [16], a modified version of NMAR that we implemented in MATLAB. FSMAR combines the image reconstructed using NMAR with one reconstructed from the original data by convolving both images with low and high-pass Gaussian filters. The final image is obtained from com-

bining the low-pass filtered NMAR image with a spatially weighted average of the high-pass filtered NMAR and original images; the original image is weighted more heavily in the neighborhood of the metal regions. As the goal of FSMAR is similar to that of wPSART-PICS (to restore details lost from the NMAR process), it is a natural point of comparison.

In addition to a qualitative assessment of the images, we computed PSNR values over the entire images similarly to the previous experiment, using the following procedure. First, the pixel values in all images were clipped using the formula

$$x_k = \min(\max(x_k, x_{min})x_{max}) \qquad (19)$$

for all k, with $x_{min} = 0.15$ cm^{-1}, $x_{max} = 0.4$ cm^{-1}. PSNR was then calculated as in (16) and (18). The rationale is that when assessing image quality, we are primarily interested in how well the different algorithms reconstruct values for soft tissue and bone; clipping the images avoids discrepancies in the reconstructed values for metal from having a disproportionate effect on the PSNR calculation.

Reconstructed images of the four phantoms are shown in Fig. 4 and Fig. 5. We focus on the first three images here, and discuss the fourth (head phantom) at end of the section. Row C of the figures shows the prior images reconstructed from the NMAR data. It is apparent in Fig. 5 that some information has been lost due to the interpolation performed by NMAR; for example, the area around the spine and backmost ribs in the abdomen image, the scapula on the right side of the shoulder image, and the edges of the hip bones in the pelvis image. While the wPSART-TV algorithm (Row D) does a better job of recovering these features, streaking artifacts caused by metal persist in every image, most noticeably between the two implants in the hip image. The three images reconstructed using wPSART-PICS (rows F–H) are able to eliminate streaks caused by metal while also recovering features which were occluded in the prior image. The PSNR values in Table II confirm these observations; the highest values for the abdomen, shoulder and pelvis phantoms all occur in column F, with columns G and H being only slightly worse. As in the simple phantom experiment, there is little apparent difference in the images reconstructed using $\alpha < 1.0$ (rows G and H), while the image using $\alpha = 1.0$ (i.e., TV as the penalty function) is noticeably smoother. In the abdomen and shoulder images, including the prior in the penalty function has actually introduced some mild streaking into the image along the horizontal direction, since these streaks are also present in the prior image. We also observe some small dark shadows surrounding the metal regions, similar to the simple phantom experiment.

The results using water corrected data (image E) indicate that the proposed method can still give improved results when the spectrum is not known. In particular, the abdomen and shoulder images in Row E are quite similar to the corresponding images in Rows F – G which

were obtained using the polyenergetic version of the algorithm, although the PSNR values in Table II suggest that they are somewhat less accurate. For the pelvis image, a noticeable streaking artifact persists between the two hip implants. The results using FSMAR (image I) indicate that it is effective in recovering some details which are lost in the NMAR image, such as the ribs in the abdomen image and the scapula in the shoulder image. Those features appear blurrier, however, than in the images reconstructed using wPSART-PICS. Curiously, the PSNR values for FSMAR (Table II) are the worst of any algorithm for the abdomen, shoulder and pelvis phantoms, despite the fact that the images appear visually superior to those in rows C – E, in most cases. Examining the difference images between reconstructed images and the ground truth, it appears that this is because FSMAR has created some halo-like regions of elevated attenuation surrounding the metal objects, which are larger than in the other images. It is possible that fine-tuning the choice of frequency cutoff and weighting functions used in the method could reduce this effect.

It is apparent that the wPSART-PICS algorithm does not give an acceptable reconstructed image in the case of the head phantom (last column of Fig. 4). The reason for this is that the metal simulated in the head phantom experiment (gold) has such a high μ value that the three objects modeling dental fillings block all X-rays passing through them at the simulated count rate of 2.0×10^5 counts per ray. This results in a measured intensity of $I_j = 0$, translating to infinite attenuation along the line. Due to the projection weighting employed by the algorithm (11), these measurements are ignored during reconstruction; however, the lack of information about pixel intensities along those lines produce artifacts in the final image. The artifacts are actually more severe in the images which begin with the prior as an initial estimate (Rows F–H); this is because there is a slight mismatch between the metal trace in the forward projection of the prior image and that of the measured sinogram, which creates severe streaking in the reconstructed image after just one iteration of the algorithm. Based on the quantitative results in Table II, the wPSART-TV (column D) produces the best reconstruction for this image, though it includes some streaking which is less severe or absent in the images reconstructed using NMAR and FSMAR.

IV. DISCUSSION

While the wPSART-PICS algorithm was effective in removing metal artifacts in most cases, the numerical experiments do highlight some limitations. In the experiment simulating gold dental fillings (fourth column of Fig. 4), the algorithm failed to produce acceptable results, due to the total photon starvation induced by the dense metal objects. In a separate experiment (not shown), we simulated titanium fillings rather than gold; this eliminated the artifacts as the titanium fillings no

longer blocked all X-rays. Additionally, we note that the simulated sinogram data for the pelvis phantom also included measurements along which no photons were detected; nonetheless, the wPSART-PICS algorithm was successfully able to reconstruct this image. As indicated in Fig. 6, the key difference appears to be that not *all* measurements through the metal objects in the pelvis phantom are totally attenuated; only those passing through both objects. Thus, the algorithm is able to reconstruct the object accurately based on the remaining information. We conclude that while the wPSART-PICS algorithm is able to perform well in challenging scenarios including some photon starvation, the NMAR or FSMAR algorithms may be preferable in cases where extreme photon starvation occurs. It should be noted that our simulations do not include scatter, which would potentially have an impact as the measured intensity I_j would no longer be zero in cases of photon starvation.

Additional limitations include the need to tune parameters such as N, γ, i_{max} and/or ε in Algorithm 4 to obtain good results, and the use of spectral knowledge in the forward projection step (9), which may not always be available. Our experiments indicate that in the event that the beam spectrum is unknown, it may be possible to use water corrected data with a monoenergetic version of the algorithm and still obtain qualitatively similar images. Alternatively, one may consider applying more advanced corrections to the data which attempt to compensate for second-order beam hardening artifacts (e.g. [37,38]). These approaches often require segmenting the image, which is not a significant obstacle since this is already required for NMAR.

Our numerical experiments have included a comparison with our own implementation of FSMAR, which also aims to recover details lost during the NMAR process. The experiments indicate that FSMAR is able to recover many such details, though they appeared somewhat blurrier than those obtained using wPSART-PICS. The performance of FSMAR does depend on the choice of frequency cutoff used for the low-pass filtering, as well as the weighting method used, so it is likely that our results could be improved upon. FSMAR has the advantage of using conventional analytical techniques for reconstruction, which are faster than iterative approaches, and it has been successfully applied in clinical practice [53]. The wPSART-PICS algorithm as currently implemented is somewhat time consuming as it uses an explicitly formed system matrix from the MIRT toolbox to perform forward and back projection on the CPU; the algorithm could be accelerated significantly through the use of GPU based forward projection. It is also possible that a prior reconstructed using FSMAR could be used in our algorithm, instead of the NMAR image.

The presented algorithm is similar to one used in a clinical study [17], which was also based on combining NMAR with a PICCS-like approach. Some differences in our approach include the use of a polyenergetic forward model and the incorporation of the superiorization methodology, which provides some theoretical benefits. For example, if one wishes to obtain an image satisfying a certain measure of data fidelity, superiorization guarantees that this is possible if the algorithm is perturbation resilient. Our previous work with the polyenergetic version of SART [47] indicates that the algorithm seems to satisfy this property.

In recent years there has been considerable interest in applying techniques from deep learning to many areas of CT imaging, including MAR (e.g. [14]). One challenge of deep learning approaches is the need for large amounts of data on which to train the network. For MAR in clinical CT, this may be a particular challenge as it is not generally possible to obtain (real) paired training data of metal and non-metal corrupted images for supervised learning, thus requiring either simulated data, or an unsupervised approach. It may also be advantageous for deep learning-based MAR approaches to incorporate existing analytic or iterative methods for MAR, as in [14].

V. CONCLUSION

In this paper we present an iterative reconstruction algorithm for CT imaging which uses the superiorization methodology to perform metal artifact reduction (MAR). The algorithm uses a prior image reconstructed using the normalized metal artifact reduction (NMAR) method of Meyer et al. [15], which eliminates most severe streaking artifacts caused by metal, but may introduce secondary artifacts in the vicinity of the metal regions. The NMAR-based prior is then incorporated into a penalty function akin to that used in prior image constrained compressive sensing (PICCS) algorithms [50], which is used within a superiorized iterative algorithm based on our previous work (wPSART-TV) [44]. Numerical experiments modeling several different anatomical scenarios were perfomed, and indicate that the proposed algorithm (wPSART-PICS) is able improve on both NMAR and wPSART-TV. In particular, it is able to recover details that are lost during the NMAR process (particularly with respect to the structure of bone around the metal regions) while also removing streaking artifacts that persist in images reconstructed using wPSART-TV.

ACKNOWLEDGMENTS

[1] B. De Man, J. Nuyts, P. Dupont, G. Marchal, and P. Suetens, Metal streak artifacts in X-ray computed tomography: a simulation study, in *Nuclear Science Symposium, 1998. Conference Record. 1998 IEEE*, volume 3, pages 1860–1865, IEEE, 1998.

[2] L. Gjesteby, B. De Man, Y. Jin, H. Paganetti, J. Verburg, D. Giantsoudi, and G. Wang, Metal artifact reduction in CT: where are we after four decades?, IEEE Access **4**, 5826–5849 (2016).

[3] F. Bamberg, A. Dierks, K. Nikolaou, M. F. Reiser, C. R. Becker, and T. R. Johnson, Metal artifact reduction by dual energy computed tomography using monoenergetic extrapolation, European radiology **21**, 1424–1429 (2011).

[4] G. H. Glover and N. J. Pelc, An algorithm for the reduction of metal clip artifacts in CT reconstructions, Medical physics **8**, 799–807 (1981).

[5] W. A. Kalender, R. Hebel, and J. Ebersberger, Reduction of CT artifacts caused by metallic implants., Radiology **164**, 576–577 (1987).

[6] J. Müller and T. M. Buzug, Spurious structures created by interpolation-based CT metal artifact reduction, in *Medical Imaging 2009: Physics of Medical Imaging*, volume 7258, page 72581Y, International Society for Optics and Photonics, 2009.

[7] M. Bal and L. Spies, Metal artifact reduction in CT using tissue-class modeling and adaptive prefiltering, Medical physics **33**, 2852–2859 (2006).

[8] D. Prell, Y. Kyriakou, M. Beister, and W. A. Kalender, A novel forward projection-based metal artifact reduction method for flat-detector computed tomography, Physics in Medicine & Biology **54**, 6575 (2009).

[9] S. Karimi, P. Cosman, C. Wald, and H. Martz, Segmentation of artifacts and anatomy in CT metal artifact reduction, Medical physics **39**, 5857–5868 (2012).

[10] C. Lemmens, D. Faul, and J. Nuyts, Suppression of metal artifacts in CT using a reconstruction procedure that combines MAP and projection completion, IEEE transactions on medical imaging **28**, 250–260 (2009).

[11] J. M. Verburg and J. Seco, CT metal artifact reduction method correcting for beam hardening and missing projections, Physics in Medicine & Biology **57**, 2803 (2012).

[12] Y. Zhang, H. Yan, X. Jia, J. Yang, S. B. Jiang, and X. Mou, A hybrid metal artifact reduction algorithm for x-ray CT, Medical physics **40** (2013).

[13] Z. Tang, G. Hu, and H. Zhang, Efficient metal artifact reduction method based on improved total variation regularization, J Med Biol Eng **34**, 261–268 (2013).

[14] Y. Zhang and H. Yu, Convolutional Neural Network based Metal Artifact Reduction in X-ray Computed Tomography, IEEE transactions on medical imaging **37**, 1370–1381 (2018).

[15] E. Meyer, R. Raupach, M. Lell, B. Schmidt, and M. Kachelrieß, Normalized metal artifact reduction (NMAR) in computed tomography, Medical physics **37**, 5482–5493 (2010).

[16] E. Meyer, R. Raupach, M. Lell, B. Schmidt, and M. Kachelrieß, Frequency split metal artifact reduction (FSMAR) in computed tomography, Medical physics **39**, 1904–1916 (2012).

[17] P. Bannas, Y. Li, U. Motosugi, K. Li, M. Lubner, G.-H. Chen, and P. J. Pickhardt, Prior image constrained compressed sensing metal artifact reduction (PICCS-MAR): 2D and 3D image quality improvement with hip prostheses at CT colonography, European radiology **26**, 2039–2046 (2016).

[18] J. Wei, L. Chen, G. A. Sandison, Y. Liang, and L. X. Xu, X-ray CT high-density artefact suppression in the presence of bones, Physics in Medicine & Biology **49**, 5407 (2004).

[19] O. Watzke and W. A. Kalender, A pragmatic approach to metal artifact reduction in CT: merging of metal artifact reduced images, European radiology **14**, 849–856 (2004).

[20] F. E. Boas and D. Fleischmann, Evaluation of two iterative techniques for reducing metal artifacts in computed tomography, Radiology **259**, 894–902 (2011).

[21] B. Kratz, I. Weyers, and T. M. Buzug, A fully 3D approach for metal artifact reduction in computed tomography, Medical physics **39**, 7042–7054 (2012).

[22] S. Zhao, D. Robertson, G. Wang, B. Whiting, and K. T. Bae, X-ray CT metal artifact reduction using wavelets: an application for imaging total hip prostheses, IEEE transactions on medical imaging **19**, 1238–1247 (2000).

[23] A. Mehranian, M. R. Ay, A. Rahmim, and H. Zaidi, X-Ray CT metal artifact reduction using wavelet domain L_0 sparse regularization, IEEE transactions on medical imaging **32**, 1707–1722 (2013).

[24] P. Babaheidarian and D. Castañón, A Randomized Approach to Reduce Metal Artifacts in X-Ray Computed Tomography, Electronic Imaging **2017**, 24–29 (2017).

[25] L. Gjesteby, H. Shan, Q. Yang, Y. Xi, B. Claus, Y. Jin, B. De Man, and G. Wang, Deep Neural Network for CT Metal Artifact Reduction with a Perceptual Loss Function, in *Fifth international conference on image formation in X-ray computed tomography*, 2018.

[26] W. J. Veldkamp, R. M. Joemai, A. J. van der Molen, and J. Geleijns, Development and validation of segmentation and interpolation techniques in sinograms for metal artifact suppression in CT, Medical physics **37**, 620–628 (2010).

[27] G. Wang, D. L. Snyder, J. A. O'Sullivan, and M. W. Vannier, Iterative deblurring for CT metal artifact reduction, IEEE transactions on medical imaging **15**, 657–664 (1996).

[28] B. De Man, J. Nuyts, P. Dupont, G. Marchal, and P. Suetens, An iterative maximum-likelihood polychromatic algorithm for CT, IEEE transactions on medical imaging **20**, 999–1008 (2001).

[29] K. Van Slambrouck and J. Nuyts, Metal artifact reduction in computed tomography using local models in an image block-iterative scheme, Medical physics **39**, 7080–7093 (2012).

[30] M. Oehler and T. Buzug, Statistical image reconstruction for inconsistent CT projection data, Methods of information in medicine **46**, 261–269 (2007).

[31] L. Ritschl, F. Bergner, C. Fleischmann, and M. Kachelrieß, Improved total variation-based CT image reconstruction applied to clinical data, Physics in Medicine & Biology **56**, 1545 (2011).

[32] X. Zhang, J. Wang, and L. Xing, Metal artifact reduction in x-ray computed tomography (CT) by constrained optimization, Medical physics **38**, 701–711 (2011).

[33] Z. Chang, D. H. Ye, S. Srivastava, J. Thibault, K. Sauer,

and C. Bouman, Prior-Guided Metal Artifact Reduction for Iterative X-Ray Computed Tomography, IEEE Transactions on Medical Imaging **38**, 1532–1542 (2019).

[34] G. T. Herman, E. Garduño, R. Davidi, and Y. Censor, Superiorization: An optimization heuristic for medical physics, Medical Physics **39**, 5532–5546 (2012).

[35] R. A. Brooks and G. Di Chiro, Beam hardening in X-ray reconstructive tomography, Phys. Med. Biol. **21**, 390–398 (1976).

[36] P. M. Joseph and R. D. Spital, A Method for Correcting Bone Induced Artifacts in Computed Tomography, Journal of Computer Assisted Tomography **2**, 100–108 (1978).

[37] P. Joseph and C. Ruth, A method for simultaneous correction of spectrum hardening in CT images containing both bone and iodine, Med. Phys. **24** (1997).

[38] Y. Kyriakou, E. Meyer, D. Prell, and M. Kachelrieß, Empirical beam hardening correction (EBHC) for CT, Med. Phys. **37**, 5179–5187 (2010).

[39] I. A. Elbakri and J. A. Fessler, Statistical Image Reconstruction for Polyenergetic X-ray Computed Tomography, IEEE Trans. Med. Imag. **21**, 89–99 (2002).

[40] G. Van Gompel, K. Van Slambrouck, M. Defrise, K. Batenburg, J. de Mey, J. Sijbers, and J. Nuyts, Iterative correction of beam hardening artifacts in CT, Med. Phys. **38**, S36–S49 (2011).

[41] Y. Lin and E. Samei, An efficient polyenergetic SART (pSART) reconstruction algorithm for quantitative myocardial CT perfusion, Medical physics **41** (2014).

[42] A. H. Andersen and A. C. Kak, Simultaneous algebraic reconstruction technique (SART): a superior implementation of the ART algorithm, Ultrasonic Imaging **6**, 81–94 (1984).

[43] Y. Censor and T. Elfving, Block-Iterative Algorithms with Diagonally Scaled Oblique Projections for the Linear Feasibility Problem, SIAM Journal on Matrix Analysis and Applications **24**, 40–58 (2002).

[44] T. Humphries and A. Gibali, Superiorized polyenergetic

reconstruction algorithm for reduction of metal artifacts in CT images, in *2017 IEEE Nuclear Science Symposium Conference Record*, 2017.

[45] Y. Lin and E. Samei, An efficient polyenergetic SART (pSART) reconstruction algorithm for quantitative myocardial CT perfusion, Med. Phys. **41**, 021911–1 – 021911–14 (2014).

[46] T. Humphries, Technical Note: Convergence analysis of a polyenergetic SART algorithm, Medical Physics **42**, 1407–1404 (2015).

[47] T. Humphries, J. Winn, and A. Faridani, Superiorized algorithm for reconstruction of CT images from sparse-view and limited-angle polyenergetic data, Phys. Med. Biol. **62**, 6762 (2017).

[48] P. Sukovic and N. Clinthorne, Penalized weighted least-squares image reconstruction for dual energy X-ray transmission tomography, IEEE Trans. Med. Imag. **19**, 1075–1081 (2000).

[49] Y. Censor, G. T. Herman, and M. Jiang, Special Issue on Superiorization: theory and applications, Inverse Problems **33** (2017).

[50] G.-H. Chen, J. Tang, and S. Leng, Prior image constrained compressed sensing (PICCS): a method to accurately reconstruct dynamic CT images from highly undersampled projection data sets, Med. Phys. **35**, 660–663 (2008).

[51] P. T. Lauzier, J. Tang, and G.-H. Chen, Time-resolved cardiac interventional cone-beam CT reconstruction from fully truncated projections using the prior image constrained compressed sensing (PICCS) algorithm, Phys. Med. Biol. **57**, 2461 (2012).

[52] J. Fessler, Michigan Image Reconstruction Toolbox. `http://web.eecs.umich.edu/~fessler/code/`.

[53] F. Morsbach, S. Bickelhaupt, G. A. Wanner, A. Krauss, B. Schmidt, and H. Alkadhi, Reduction of metal artifacts from hip prostheses on CT images of the pelvis: value of iterative reconstructions, Radiology **268**, 237–244 (2013).
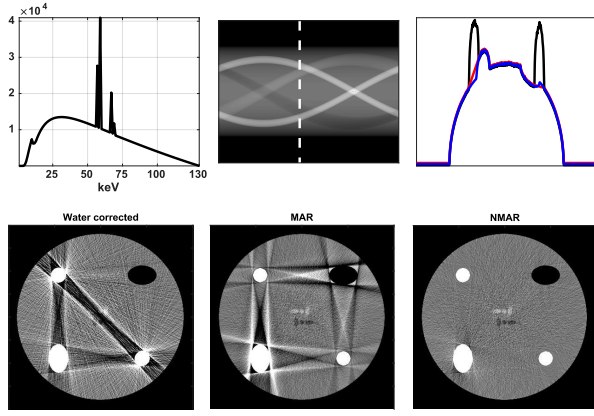
FIG. 1. Illustration of MAR and NMAR methods. Top row: Left: Spectrum (130 kVp) used to generate polyenergetic data. Center: polyenergetic sinogram of a simple mathematical phantom including metal objects (small circular regions) as well as bone (oblong region in bottom right) and air pocket (top right). Right: Profile along white dashed line in sinogram, showing water corrected sinogram (black line), MAR correction (red line) and NMAR correction (blue line). Profiles have been vertically offset to highlight differences. Bottom: Images reconstructed from water corrected (left), MAR corrected (center) and NMAR corrected (right) sinograms using filtered backprojection. Phantom specifications are given in Section III.
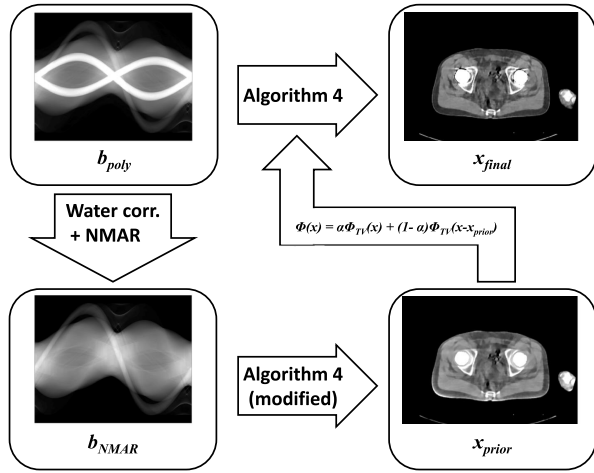

FIG. 2. Scheme of the wPSART-PICS algorithm as described in Algorithm 5. Raw data b_{poly} are water corrected, then passed into NMAR (Algorithm 3) to generate a metal corrected sinogram b_{NMAR}. This sinogram is used to generate the prior image x_{prior}, which is then incorporated into the penalty function in Algorithm 4 to produce the final output x_{final}.
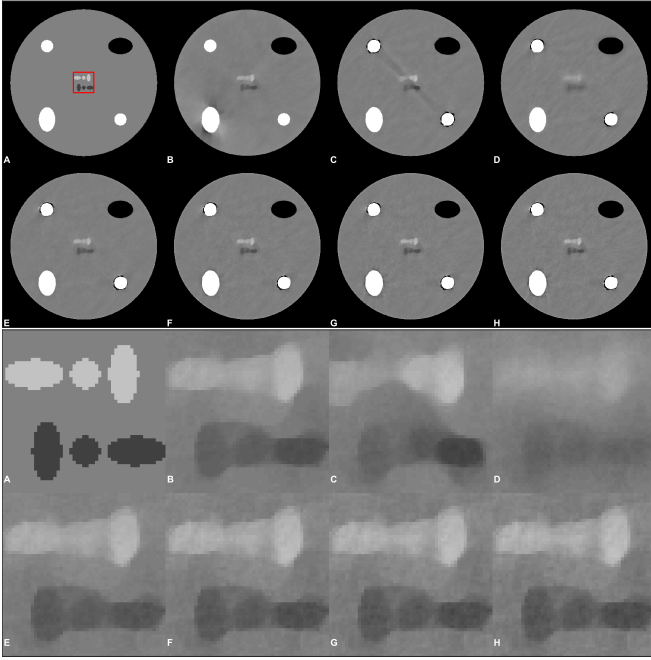
FIG. 3. Images reconstructed at noise level of $I_0 = 5.0 \times 10^5$. A: True image. B: Prior image x_{prior} reconstructed from NMAR data. C: Image reconstructed using wPSART-TV. D – H: Images reconstructed using wPSART-PICS with $\alpha = 1.0, 0.8, 0.5, 0.2$ and 0.0, respectively. Top two rows: full image; bottom two rows: zoomed in on ROI highlighted in red box. Grayscale window is $\pm10\%$ the value of the soft tissue background.

TABLE I. PSNR values of reconstructed images within the ROI shown in Fig. 3. Column headings refer to images shown in Fig. 3.

Counts	B	C	D	E	F	G	H
1.0e5	21.36	21.41	21.24	21.73	21.92	21.97	21.97
2.0e5	21.96	22.00	21.30	22.35	22.49	22.58	22.62
5.0e5	23.28	22.24	21.37	23.56	23.82	23.93	23.97
1.0e6	23.95	20.46	21.67	24.20	24.52	24.62	24.66

TABLE II. PSNR values of reconstructed images shown in Fig. 4. Column headings refer to images shown in Fig. 4.

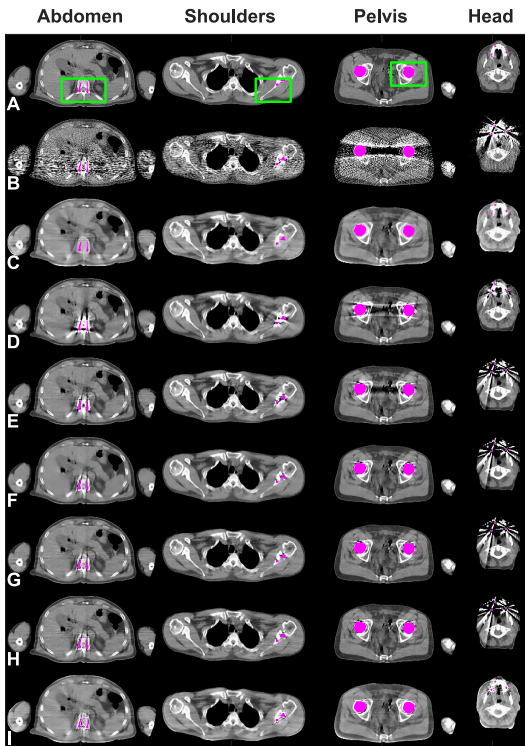| Phantom	C	D	E	F	G	H	I
Abdomen	27.06	26.47	29.18	30.79	30.69	30.58	25.65
Shoulders	28.21	28.16	30.34	32.65	32.45	32.35	27.78
Pelvis	27.35	26.69	28.36	29.67	29.63	29.59	25.20
Head	23.87	25.81	18.84	18.82	18.79	18.80	22.38

FIG. 4. Phantoms and reconstructions based on clinical CT image slices. Row A: True phantoms at reference energy of 70 keV with metal inserts indicated in pink. Row B: reconstructions generated using FBP and water corrected data. Row C: Prior images reconstructed from NMAR data. Row D: Images reconstructed using wPSART-TV. Row E: Image reconstructed using modified wPSART-PICS and water corrected data. Rows F–H: Images reconstructed using wPSART-PICS with $\alpha = 1.0, 0.5$ and 0.0, respectively. Row I: Images reconstructed using FSMAR. Grayscale window is $[0.15, 0.25]$ cm^{-1}. Images were reconstructed at 512×512 pixels, but have been cropped to eliminate black space. Green boxes indicate zoomed-in regions shown in Fig. 5.
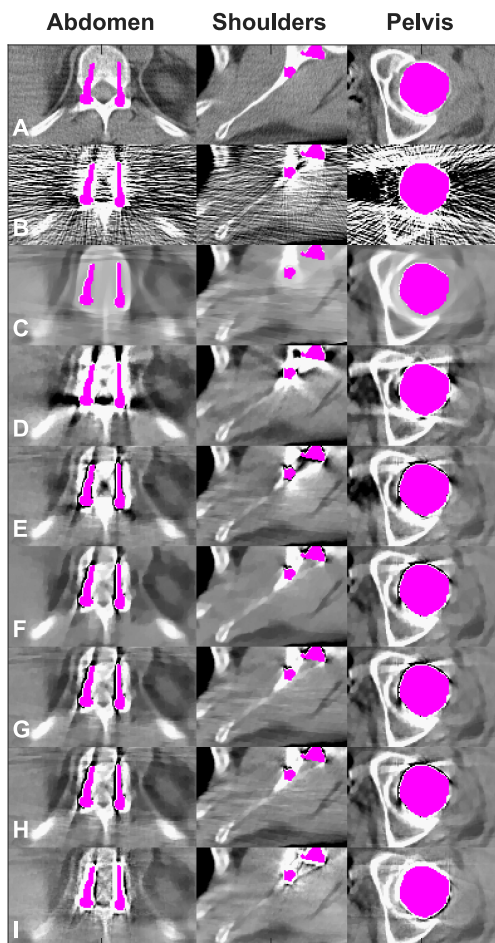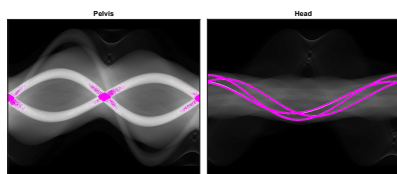
FIG. 5. Zoomed-in regions indicated in Fig. 4.

FIG. 6. Fan-beam sinograms corresponding to pelvis and head phantoms with initial count rate of $I_0 = 2.0 \times 10^5$. Measurements corresponding to infinite attenuation are shown in pink.